Computers and Concrete, Vol. 9, No. 4 (2012) 293-310
DOI: http://dx.doi.org/10.12989/cac.2012.9.4.293

The high-rate brittle microplane concrete model: Part I: bounding curves and quasi-static fit to material property data

Mark D. Adley*, Andreas O. Frank and Kent T. Danielson

U.S. Army Engineer Research and Development Center
Impact and Explosive Effects Branch, ATTN: CEERD-GM-I 3909 Halls Ferry Road
Vicksburg, MS 39180-6199 USA

(Received July 3, 2010, Revised June 13, 2011, Accepted June 14, 2011)

Abstract. This paper discusses a new constitutive model called the high-rate brittle microplane (HRBM) model and also presents the details of a new software package called the Virtual Materials Laboratory (VML). The VML software package was developed to address the challenges of fitting complex material models such as the HRBM model to material property test data and to study the behavior of those models under a wide variety of stress- and strain-paths. VML employs Continuous Evolutionary Algorithms (CEA) in conjunction with gradient search methods to create automatic fitting algorithms to determine constitutive model parameters. The VML code is used to fit the new HRBM model to a well-characterized conventional strength concrete called WES5000. Finally, the ability of the new HRBM model to provide high-fidelity simulations of material property experiments is demonstrated by comparing HRBM simulations to laboratory material property data.

Keywords: constitutive modeling; optimization algorithms; microplane models.

1. Introduction

The Geotechnical and Structures Laboratory of the U.S. Army Engineer Research and Development Center (ERDC) have conducted a significant amount of projectile penetration research. These efforts included numerous projectile penetration experiments using the ERDC 83 mm ballistic research facility (Frew *et al.* 1993), extensive material property experiments that characterize target mechanical behavior and provide data for fitting constitutive models (Akers *et al.* 1995), and numerous first-principle calculations of various penetration events (Adley *et al.* 2010). Our research is focused around gathering data and gaining insight into the processes of penetration mechanics. To reach these goals, a significant part of our research is to develop more accurate and robust material models.

In this paper, we describe an effort to produce a microplane model (Bazant *et al.* 1996a, 1996b, 2000, Caner and Bazant 2000, Ozbolt *et al.* 2005, 2008) with exceptional resolution for highly impulsive boundary value problems of interest. More specifically, we focused our efforts on projectile perforation of conventional strength concrete slabs. Our goal is to develop a high-resolution Microplane model that can be fit to various quasi-static material property data and then used in a variety of projectile perforation calculations. In order to accomplish that goal, we started with the M4 microplane model

* Corresponding author, Ph. D., E-mail: mark.d.adley@usace.army.mil

(Bazant *et al.* 2000, Caner and Bazant 2000) as a framework to build upon. The M4 model has typically provided very reasonable results for the target damage caused by projectile penetration, embedded detonation and blast-related problems (Danielson *et al.* 2010, Littlefield *et al.* 2010). However, the authors observed that the model has difficulty predicting accurate exit velocities for projectile perforation problems, especially when the target thickness approaches the perforation limit thickness, i.e., the exit velocity is very small. We attempted to address this issue by increasing the resolution of the M4 microplane model through the introduction of additional bounding curves. We called this form of the model the High-Rate Brittle Microplane model (HRBM).

We will show that the HRBM model has significantly increased the resolution for fitting our material property data. The HRBM model also provides an increased level of flexibility that will be required to fit emerging high-strength concrete materials that contain glass (Roth *et al.* 2010) and steel fibers (Williams *et al.* 2010). However, this also greatly increased the complexity of the model and further increased the difficulties of fitting the model. Due to the increased level of complexity for HRBM, it may be prohibitively difficult to fit the model, which can render the model practically unusable without some sort of automated fitting procedure. This hurdle was overcome by developing a material driver code and an automatic fitting code to help search for acceptable material constants (Adley *et al.* 2010). In this paper, we discuss both the HRBM model and the numerical algorithms used in the VML code to fit the model. We also present the quasi-static material fit to a given conventional strength concrete known as WES-5000. In a companion paper (Frank *et al.* 2010), we more thoroughly exercise the HRBM model and its material fit to WES-5000 by conducting numerous projectile perforation calculations.

2. HRBM-Microplane model

2.1 Model description

We used the M4 microplane model (Bazant *et al.* 2000, Caner and Bazant 2000) as a framework for the HRBM model. Thereby, the basic model remained unchanged and we shall not describe it herein. However, we introduced an additional set of bounding curves into the M4 model framework. Thereby the HRBM model includes both the original M4 bounding curves as well as additional bounding curves designed to increase the model's fidelity. This combination of bounding curves provided greater resolution and flexibility in fitting our material property data. For example, the original M4 bounding curves and their inherent scaling, i.e., using the "free" parameters such as E and k's, retain the clever simplicity of fitting the HRBM model to various conventional data, i.e., unconfined strengths near 5 ksi. When using the original M4 bounding curves with the HRBM model, only the free parameters need to be changed to produce slight variations in the material responses. However, we noticed that the resolution of M4 fits to our specific material property data was not adequate in many cases. For example, we observed that it was difficult to produce a high-resolution fit using only the M4 bounding curves, especially when different concrete materials show significant differences in hydrostatic response as well as unconfined compressive strength. We believe the reason for this behavior is that the original M4 bounding curves do not have sufficient resolution to capture some of the relevant material behavior we have observed. In order to address this issue and obtain a higher resolution material fit, the additional HRBM bounding curves were designed to better capture the hydrostatic material response as well as the material triaxial behavior

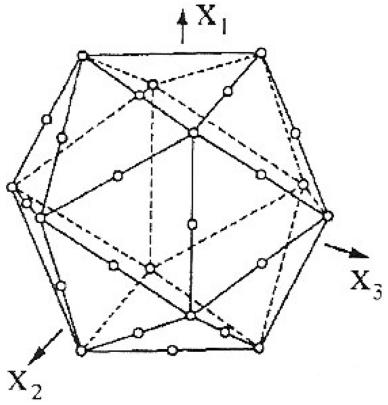

Fig. 1 Microplanes distributed over a unit sphere composed of 21 individual planes (Bazant and Oh 1986)

at low confining pressures, i.e., brittle response. Nonetheless, it should be cautioned that the additional HRBM bounding curves have no inherent scaling, which can greatly increase the difficulty in fitting the model.

The microplane bounding curves provide the limiting stress states for each individual microplane. The integration of these microplanes over a sphere provides the rich interaction between the individual planes in order to produce the "global" macroscopic response of the material (Fig. 1). The microplane model was designed to provide various bounding curves that locally limit a specific stress state or material response on a given plane, described as follows. The volumetric boundary representing compressive pore collapse and subsequent locking of the material, the frictional yield boundary curve representing sliding frictional strength, i.e., the "ductile" shearing response of the material and the deviatoric shear boundaries representing spreading in compression and splitting in extension. These boundaries dominate the low-pressure triaxial behavior and represent the cohesive strength of the material. The tensile normal boundary represents pure tensile cracking and crack closing. The material response for stress states beneath each bounding curve is linear elastic; however, the stress state must not exceed the bounding curves and is thereby forced to locally follow each curve on a given plane, which becomes highly non-linear.

Due to inherent spherical geometry of the model (Fig. 1) and the individual stress versus strain responses on each plane, it is likely that different bounding curves become engaged on different microplanes during a given "global" stress path. For example, during an unconfined compression test, the microplanes lateral to the central axis (or loading axis) may be dominated by the compressive deviatoric boundary, whereas the lateral microplanes may be dominated by the tensile normal boundary due to the Poisson effect. Fig. 2 shows the variations in the responses on each microplane during an unconfined compression test. Due to the symmetry of the 28-plane sphere, many of the resulting stress versus strain responses on a given microplane are the same. Notice that the integration of these different responses produces the global material response (Bazant and Oh 1986). These complex interactions can then produce a very rich material response that may inherently capture a wide variety of different material behaviors, such as the Poisson effect described above.

It should be noted that our intended application for the HRBM model are projectile perforation events. These events typically produce high-pressures over a small region under the nose of the

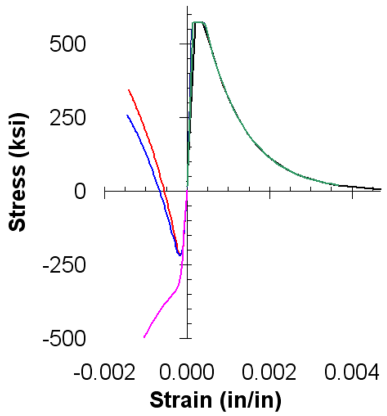

Fig. 2 Variations in the responses of each microplane during an unconfined compression test. Shown are the microplane stress versus strain for each plane from a 28-plane sphere

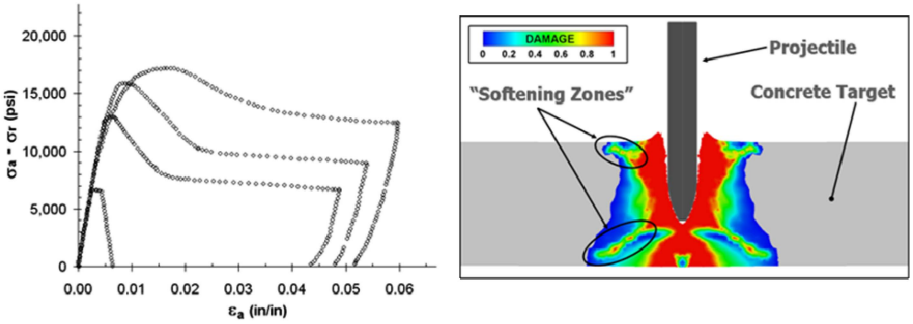

(a) (b)

Fig. 3 The material "softening" response observed in concrete. (a) Post-peak softening from stress versus strain TXC lab data at low pressures (<20 MPA), (b) Localized "shear bands" or "softening zones" that develop during a projectile perforation event due to the material softening response (Frank and Adley 2007)

projectile as it penetrates the target; however, the majority of the target response is dominated by the low-pressure "brittle" behavior of concrete (Frank and Adley 2007). Furthermore, this "brittle" or "softening" behavior of the material is dominated by the tensile normal and deviatoric boundaries. Hence, it is imperative to accurately capture this behavior in order to properly model projectile perforation events. Fig. 3 shows the "softening" behavior of the low-pressure triaxial-compression (TXC) material property data as well as the resulting "shear bands" that arise in a perforation calculation due to this material "softening" response. Notice that accurate modeling of the material softening behavior may be required in order to adequately predict the material damage, i.e., impact and exit craters, as well as the projectile exit velocity during such a perforation event.

2.2 Volumetric boundaries

The volumetric boundary provides the limiting volumetric stress (σ_v) for all microplanes as a function of volumetric strain (ε_v). The HRBM model retains the original M4 compressive volumetric boundary, i.e.,

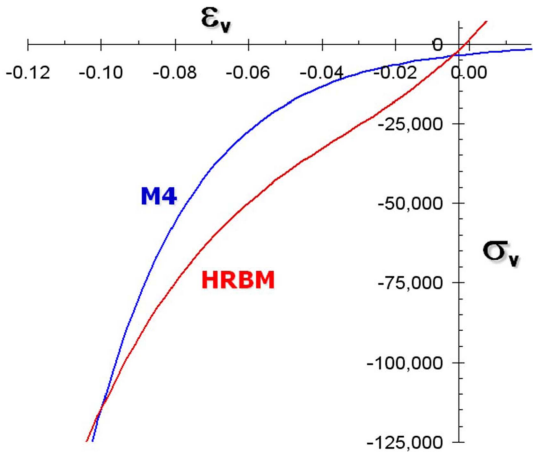

Fig. 4 The compressive volumetric bounding curves for the original M4 model (blue) and the HRBM model (red) as fitted to WES-5000 concrete

negative volume strain. The M4 boundary is

$$\sigma_v = -Ek_1k_3 \quad \exp(\varepsilon_v / k_1k_4) \tag{1}$$

where E is the elastic modulus, and k_1, k_3 and k_4 are free material parameters. The exponential form of the original M4 volumetric compressive boundary provides a reasonable fit to a wide variety of the data presented in the literature, however, it does not have the required fidelity to provide a high-resolution fit to our material property data. Therefore, we considered a cubic polynomial, which seems to better approximate the volumetric crushing response of the material, i.e., void closure. In addition to Eq. (1), the HRBM model introduces a new volumetric compressive boundary, as follows

$$\sigma_v = C_{v1} + C_{v2}\varepsilon_v + C_{v3}\varepsilon_v^2 + C_{v4}\varepsilon_v^3 \tag{2}$$

where C_{v1}, C_{v2}, C_{v3} and C_{v4} are material constants. Fig. 4 shows the compressive volumetric boundaries as fit to WES-5000 concrete.

In order to produce a better volumetric unloading response, the elastic volumetric behavior, i.e., for stress states underneath the bounding curve, was dictated to follow the unloading bulk modulus, i.e., locking modulus, as determined by high-pressure material property data. Although this may sacrifice accuracy near the toe of the volumetric response at low confining pressures, it is more likely to increase the accuracy under high levels of confinement. It should be noted that the HRBM model does not include a tensile volumetric boundary, since it has been observed that the tensile stress on a given Microplane is typically limited by the tensile normal boundary.

2.3 Frictional yield boundaries

The frictional yield boundary provides the local limiting shear stress (σ_t) on a given plane as a function of normal stress (σ_n) and volumetric strain (ε_v). The HRBM model retains the original M4 frictional yield boundary. The M4 boundary is

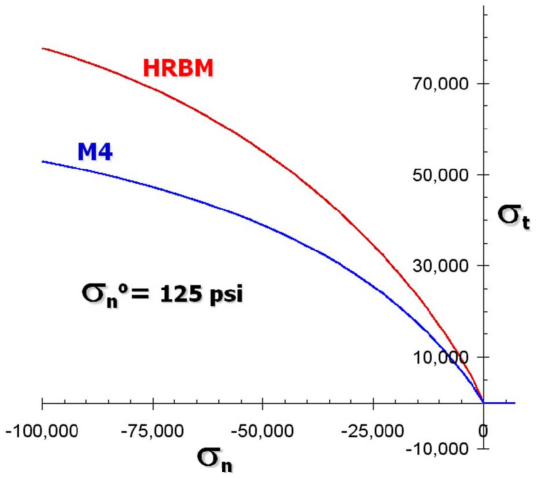

Fig. 5 The frictional shear bounding curves for the original M4 model (blue) and the HRBM model (red) as fitted to WES-5000 concrete

$$\sigma_t = \frac{Ek_1k_2c_{10}(-\sigma_n+\sigma_n^o)}{Ek_1k_2+c_{10}(-\sigma_n+\sigma_n^o)} \qquad \sigma_n^o = \frac{Ek_1c_{11}}{1+c_{12}(\varepsilon_v)} \tag{3}$$

where E is the elastic modulus, k_1 and k_2 are free material parameters and c_{10}, c_{11} and c_{12} are fixed material constants. Notice that the Macaulay brackets, defined as $\langle x\rangle = \max(x,0)$, are used here and in subsequent equations. The form of the original M4 frictional boundary provides a reasonable fit to a wide variety of the data presented in the literature; however, it does not have sufficient fidelity to provide a high-resolution fit to our material property data. Therefore, we considered a power law, which seems to better approximate the low-pressure frictional response of the material. In addition to Eq. (3), the HRBM model introduces a new frictional shear boundary, as follows

$$\sigma_t = \min(C_{s4}, C_{s1}(-\sigma_n+\sigma_n^o)+C_{s2}(-\sigma_n+\sigma_n^o)^{C_{s3}}) \qquad \sigma_n^o = \frac{C_{s5}}{1+C_{s6}(\varepsilon_v)} \tag{4}$$

where C_{s1}, C_{s2}, C_{s3}, C_{s4}, C_{s5} and C_{s6} are material constants. Fig. 5 shows the frictional yield boundaries as fit to WES-5000 concrete.

2.4 Deviatoric shear boundaries

The deviatoric shear boundaries provide the local limiting deviatoric stress (σ_d) on a given plane as a function of deviatoric strain (ε_d) and volumetric strain (ε_v). The HRBM model retains the original M4 deviatoric boundaries. The M4 compression deviatoric boundary, i.e., negative deviatoric strain, is

$$\sigma_d^- = \frac{Ek_1c_8}{1+((-\varepsilon_d-k_1c_8c_9)/k_1c_7)^2} \tag{5}$$

and the M4 extension deviatoric boundary, i.e., positive deviatoric strain, is

$$\sigma_d^+ = \frac{Ek_1c_5}{1+((\varepsilon_d-k_1c_5c_6)/k_1c_7c_{18})^2} \tag{6}$$

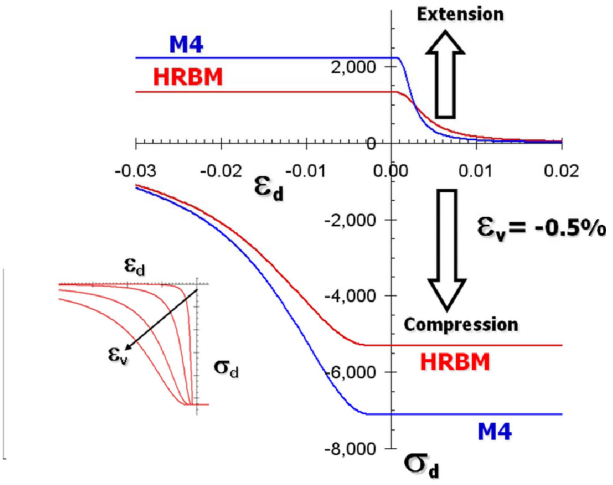

Fig. 6 The deviatoric bounding curves for the original M4 model (blue) and the HRBM model (red) as fitted to WES-5000 concrete. Also shown is the volume strain dependence (increasing e_v) for the compressive boundary

where E is the elastic modulus, k_1 is a free material parameter, and c_5, c_6, c_7, c_8, c_9 and c_{18} are fixed material constants. Notice that the form of the original M4 deviatoric boundaries (Eqs. 5-6) do not have a volume strain (ε_v) dependence. We noticed that, in order to more accurately model the pressure dependence of the cohesive strength, the deviatoric boundaries were improved if they become a function of compressive volume strain. For example, although there is typically a significant amount of cohesive strength during an unconfined compression test, this cohesive strength should gradually decrease as pressure increases and the brittle-to-ductile transition is reached, i.e., perhaps it can be assumed that there is no cohesive strength beyond the brittle-to-ductile transition. Hence, we introduced compressive volume strain dependence into the deviatoric bounding curves. In addition to Eqs. (5) and (6), the HRBM model introduces the following compression deviatoric boundary

$$\sigma_d^- = -\frac{C_{d1}}{1+(-\varepsilon_d - C_{d2}(1-(-C_{d4}\varepsilon_v))/C_{d3})^2} \tag{7}$$

and the following extension deviatoric boundary:

$$\sigma_d^+ = -\frac{C_{d6}C_{d1}}{1+(-\varepsilon_d - C_{d6}C_{d2}(1-(-C_{d5}\varepsilon_v))/(C_{d6}C_{d3}))^2} \tag{8}$$

where C_{d1}, C_{d2}, C_{d3}, C_{d4}, C_{d5} and C_{d6} are material constants. Fig. 6 shows the deviatoric boundaries as fit to WES-5000 concrete.

2.5 Tensile normal stress boundaries

The tensile normal boundary provides the local limiting positive normal stress (σ_n) on a given plane as a function of normal strain (ε_n) and volumetric strain (ε_v). The HRBM model retains the original M4 normal stress boundary. The M4 boundary is

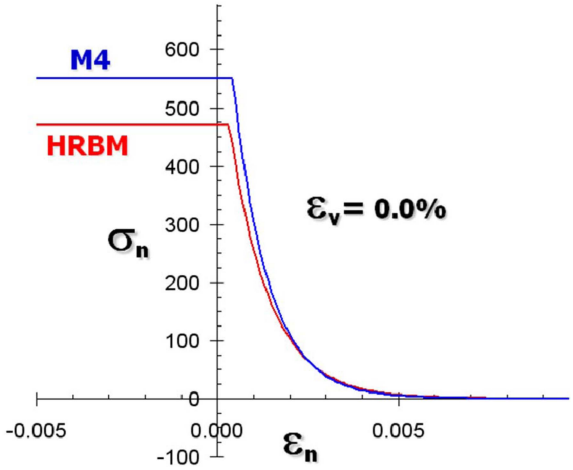

Fig. 7 The tensile normal stress bounding curves for the original M4 model (blue) and the HRBM model (red) as fitted to WES-5000 concrete

$$\sigma_n = Ek_1c_1 \exp\left(-\frac{(\varepsilon_n - k_1c_1c_2)}{k_1c_3 + (-c_4\varepsilon_v)}\right) \tag{9}$$

where E is the elastic modulus, k_1 is a free material parameter, and c_1, c_2, c_3 and c_4 are fixed material constants. We have not introduced a new tensile normal boundary curve since the original function seems to behave well for our data. However, in order to increase its flexibility, we removed the scaling (Bazant *et al.* 2000)

$$\sigma_n = C_{n1} \quad \exp\left(-\frac{(\varepsilon_n - C_{n2})}{C_{n3} + (-C_{n4}\varepsilon_v)}\right) \tag{10}$$

where C_{n1}, C_{n2}, C_{n3} and C_{n4} are material constants. Fig. 7 shows the tensile normal boundaries as fit to WES-5000 concrete.

2.6 Summary

The original M4 bounding curves were retained in the HRBM model. This allows for simple scaling of the curves in order to quickly fit conventional concrete material property data (Bazant *et al.* 2000). Notice that the free parameters E and k_1 provide a vertical and radial scaling of the bounding curves, respectively. However, also notice that all of the curves must then scale together, which greatly limits the flexibility of the response. Free parameters k_2, k_3 and k_4 allow for fine tuning the shape of the frictional yield boundary (k_2) and the compressive volumetric boundary (k_3 and k_4). The fixed parameters (c's) are not adjustable and force the shape of the bounding curves to remain similar. Hence, the original M4 bounding curves can be used to quickly obtain a fit to similar types of conventional strength concrete material but are not useful for fitting vastly different material behaviors observed in high strength concretes.

The HRBM bounding curves were designed to more accurately fit the vast differences in material properties of our data, specifically large differences in low-pressure triaxial behavior and hydrostatic behavior. Furthermore, these additional bounding curves have no inherent scaling, which allows for

much greater flexibility when fitting the material property data. The shapes and scales of these bounding curves can all be changed independently from each other. This provides exceptional resolution when fitting our material property data but comes at the cost of a significant increase in complexity. In fact, we observed that some form of automatic fitting code may be required to produce adequate material fits.

3. Material property data

3.1 Quasi-static lab data

We fit the HRBM model to the mechanical properties of a conventional strength concrete mix developed at ERDC known as WES-5000 (Cargile 1999). We used various quasi-static laboratory material characterization data to derive the material constants for our fit. The quasi-static data included unconfined compression (UC), triaxial compression (TXC), unconfined tension (UT) and uniaxial strain compression (UX). The quasi-static mechanical property tests described herein were conducted with cylindrical specimens having a nominal diameter of 2 inches and a nominal height of 4 inches. The tests were conducted at axial strain rates of approximately 10^{-4} to 10^{-5} $secs^{-1}$, i.e., from 5 to 30 minutes to peak load. All data were presented as true stresses and engineering strains. The strains were calculated as

$$\varepsilon_a = \Delta h/h_0 \qquad \varepsilon_r = \Delta d/d_0 \qquad \varepsilon_v = \varepsilon_a + 2\varepsilon_r \tag{11}$$

where ε_a is the axial strain, ε_r is the radial strain, ε_v is the volumetric strain, Δh is the change in specimen height, h_0 is the initial height, Δd is the change in specimen diameter and d_0 is the initial diameter. The stresses were calculated as

$$q = \sigma_a - \sigma_r \qquad P = (\sigma_a + 2\sigma_r)/3 \tag{12}$$

where P is the mean normal stress (or hydrostatic pressure), σ_a is the axial stress, σ_r is the radial stress and q is the principal stress difference.

4. Model fitting

This section contains a description of a software package called the Virtual Material Laboratory (VML) that was developed to determine the material model parameters for a constitutive model by providing an optimum fit to the material property data. The VML code contains a material driver code that drives the material model through various stress and strain paths used in the laboratory to characterize the material, an optimization module to determine the optimum parameter values, and a Graphical User Interface (GUI) to provide pre- and post-processing of the fits. The optimization module calls the driver code to compute predictions of a series of laboratory experiments for a given set of model parameters, it compares the predicted material response to the laboratory data, and based on the results of that comparison, it adjusts the model parameters to improve the fidelity of the model fit. The methodology used in the optimization module is discussed in the following sections.

4.1 Problem formulation

The problem of determining parameters for a constitutive model can be cast in the form of a constrained optimization problem. Specifically, the fitting algorithms are used to minimize the weighted sum of squared residuals merit function given by

$$\Phi(\bar{a}) = \sum_{i=1}^{n} w_i[\sigma_i - \hat{\sigma}_i(\varepsilon, \bar{a})]^2 \tag{13}$$

where σ_i represents the stress values measured in material property experiments, $\hat{\sigma}_i$ represents the stress values predicted by the material model that are a function of the strain (ε) and the vector of material model parameter values ($\bar{a}$), and w_i is a weighting factor, which are subject to a set of constraints, i.e., $\bar{a}_{\min} \le \bar{a} \le \bar{a}_{\max}$.

The only independent variables in Eq. (13) are the set of unknown material model parameters $\bar{a}$. Therefore, the model-fitting problem consists of selecting a set of material model parameters that minimizes the error, in a least squares sense, between the predicted stress values and the stress values measured experimentally.

The merit function represented by Eq. (13) can become extremely complex and highly non-linear due to the complexity/non-linearity of both the constitutive models and the material behaviors observed in laboratory experiments. Although direct search methods often converge quickly for well-behaved merit functions, the complexity of the merit function makes it very difficult for conventional gradient-based direct search methods to converge to an optimum solution that minimizes the aforementioned merit function. Genetic algorithms have also been used successfully in a wide range of engineering optimization problems (Parichatprecha and Nimityongskul 2009), but those methods generally involve the additional complexity of mapping between binary digit strings and discrete parameter values. For those reasons, the VML code employs continuous evolutionary algorithms or CEA (Furukawa *et al.* 2002) in conjunction with the gradient-based Levenberg-Marquardt Algorithm or LMA (Marquardt 1963). The CEA methods provide the ability to find optimum solutions for extremely complex merit functions, while the LMA approach reduces the computation time by quickly moving the candidate solutions toward the regions of the parameter space that are most likely to contain the optimum solution.

4.2 Continuous evolutionary algorithms

In CEA, a trial solution is a vector representation of the parameter set ($\bar{a}$). The algorithm employed in this work selects a number (m) of initial trial solutions where the parameter values in each of the m vectors are selected at random using a uniform distribution of values that terminate at the minimum and maximum allowable parameter values specified by the analyst. Each of the trial solutions, known as parents in CEA terminology, represents a point in the search space. Once the values of the initial set of parents are initialized, the following operations are completed in a loop: (1) Evaluation of parental fitness, (2) Direct search and (3) Recombination (mating) of parents to create a new generation. The previous three operations are computed in the order given within a loop and the loop is not terminated until a convergence criterion is satisfied, i.e., the merit function reaches an acceptably small value. In the following paragraphs, each of the three aforementioned tasks are described in greater detail.

4.3 Evaluation of parental fitness

The first step in this task is to evaluate the merit function (Φ_i) for each of the m trial solutions (parents). The maximum value of the merit function obtained for any of the parents is stored and represented here by the variable Φ_{max}. Once the value of Φ_{max} is determined, the fitness value of each parent is computed by evaluating the following equation

$$F_i = \Phi_{max} - \Phi_i \tag{14}$$

where F_i is the fitness value of the ith parent. Note that the fitness value varies from 0.0 for the least fit parent to a maximum value for the most fit parent, and that the fitness values are always greater than 0.0. During this phase of the CEA methodology, the identity (index) of the most fit parent is stored, and the identity (index) of the least fit parent is stored. The most fit parent is the best solution obtained at this point in the CEA method, and is therefore the current solution to the problem, i.e., the set of material property parameters that provides the closest prediction of the material property test data.

4.4 Direct search method

This task uses the search point that corresponds to the fittest parent as the starting point for a gradient-based search method such as the LMA. The solution computed by the direct search method is then evaluated as described in the previous step. If the fitness value is greater than the least fit parent, this new solution replaces the least fit parent. The fitness values are then recomputed, and the least and most fit parents are identified.

4.5 Recombination

This task involves recombining the existing parents to determine the next set (generation) of trial solutions. The CEA methodology presented here employs the elitist algorithm, i.e., the most fit parent (the current solution) moves to the next generation without being modified. The other (m-1) required trial solutions are obtained by a recombination process. The mating process starts by setting up a mating pool where a parent's level of participation in the mating pool depends on its merit function value (fitness). The level of a parents' participation in the mating pool is determined by evaluating the following equation

$$P_i = \frac{F_i}{\sum F_i} \tag{15}$$

where P_i is the level of representation of the parent in the mating pool. Specifically, if the size of the mating pool is 1000 and the P_i value of the ith parent is 0.10, the identity of the ith parent will be stored in 100 slots of the mating pool array. Note that the P_i value of the least fit parent is zero, i.e., the least fit solution is discarded.

After the mating pool is computed and stored, the mating process proceeds as follows. Two parents are selected at random by choosing two random numbers between 1 and 1000 (the size of mating pool) from a uniform distribution of values. The identity of the parents is stored in the slots corresponding to the two random numbers, and those parents are used in a recombination (mating) algorithm that is represented by the following equations

$$\begin{aligned} \bar{a}_i^* &= (1-\beta)\bar{a}_i + \beta\bar{a}_j \\ \bar{a}_j^* &= \beta\bar{a}_i + (1-\beta)\bar{a}_j \end{aligned} \tag{16}$$

where β is a scalar value that is defined by a normal distribution with a mean of 0 and a specified standard deviation, $\bar{a}_i^*$ and $\bar{a}_j^*$ are the new trial solutions (children), and the parents ($\bar{a}_i$ and $\bar{a}_j$) are selected at random from the mating pool as described above.

Since the probability of a solution (individual) being selected to participate in the mating process depends on the value of its merit function (level of fitness), this search algorithm moves toward a solution that minimizes the merit function and provides a best fit to the material property data used in the merit function. It is interesting to note that the CEA methods are a mathematical representation of the survival of the fittest theory. It is also clearly seen by the vocabulary used in the description of CEA algorithms that they are inspired by biological evolution processes.

As mentioned previously, the mating algorithm used in the VML code makes use of the elitist algorithm. This is useful in practice because it guarantees that the final solution will never be worse than the initial trial solution. The mating process used in the VML code also makes use of a type of mutation algorithm. In cases where the convergence has slowed or the current set of parents lack diversity, the mating pool is seeded with trial solutions (parents) that are selected at random. The process for determining the values of these trial solutions is identical to the process used to determine the values used for the initial set of parents. The mutation algorithm is useful for insuring that the search does not get stuck in a solution that is just a local minimum.

4.6 Levenberg-Marquardt Algorithm (LMA)

The direct search method chosen for inclusion in the VML code is the LMA. The LMA algorithm is an iterative method that is derived by replacing the equation for $\hat{\sigma}_i$ in Eq. (13) by the linear approximation

$$\hat{\sigma}_i(\varepsilon, \bar{a} + \bar{\alpha}) = \hat{\sigma}_i(\varepsilon, \bar{a}) + J_i\bar{\alpha} \tag{17}$$

where $\bar{\alpha}$ represents an increment in the value of $\bar{a}$. The value of J_i is defined as

$$J_i = \frac{\partial\hat{\sigma}_i(\varepsilon, \bar{a})}{\partial\bar{a}} \tag{18}$$

Substituting Eq. (17) into Eq. (13) creates a linearized version of Eq. (13). Noting that the linearized version of Eq. (13) will be a minimum when the gradient of Φ with respect to $\bar{\alpha}$ is equal to zero leads to the following set of linear equations

$$\sum_{i=1}^{n}\left(J_i^T J_i w_i + \frac{\lambda}{n}I\right)\bar{\alpha} = \sum_{i=1}^{n} J_i^T w_i(\sigma_i - \hat{\sigma}_i(\varepsilon, \bar{a})) \tag{19}$$

where λ is a damping factor, I is the identity matrix and $\bar{\alpha}$ represents an increment in the value of $\bar{a}$.

Solving the set of linear equations defined in Eq. (19) yields an increment of the parameter values that are used to compute an improved guess for an optimum solution. Specifically, the improved parameter values are computed as

$$\bar{a}_{new} = \bar{a}_{old} + \bar{\alpha} \tag{20}$$

where $\bar{a}_{new}$ is the new solution computed by the LMA method, and the value of $\bar{a}_{old}$ is set equal to the most fit parent found in the current generation of the CEA method. As stated previously, if the new solution ($\bar{a}_{new}$) proves to be more fit than the least fit parent in the current generation, it replaces the least fit parent.

4.7 Integration of LMA and CEA methods

It has been observed in a number of simulations that, in the early stages of the solution process, the LMA method often makes a significant contribution to the search for a solution. This is accomplished by seeding the population with trial solutions that are often significantly more accurate than the randomly generated trial solutions used to initialize the CEA search. Even if the initial guess is too far from the optimum for the LMA to find the solution, it still moves the CEA search towards a more promising region of space. This experience indicates that the LMA method is very useful for rapidly moving the CEA search towards the region of the parameter space that is likely to contain the optimum solution. This avoids wasting computational resources conducting CEA searches that are located in regions of the parameter space that are very unlikely to contain the optimum solution.

It has also been observed that, when the current solution is nearing the optimum solution, it is generally the CEA method that obtains an improved solution. This indicates that the CEA method is very useful for thoroughly searching a region of the parameter space that is near the optimum solution even when the merit function is very highly non-linear.

The previous two observations brought about the algorithm that is used to integrate the CEA and LMA search methods into one cohesive algorithm. The two methods are integrated in a way that attempts to use each method in the most effective manner thereby minimizing computational resources and maximizing the convergence rate. The method used to integrate the CEA and LMA methods is described below.

If the starting point (fittest parent) was obtained in the current generation, the LMA method is used with $\lambda = 0.0$, which provides a search direction that is consistent with the Gauss-Newton Algorithm. If the starting point was obtained in a previous generation, the value of λ is incremented to allow the LMA method to essentially search in a different direction. If the starting point remains constant for several generations, the value of continues λ to increase, which moves the search direction toward the gradient descent direction. If the starting point remains the same for a number of generations (currently set to 25), the LMA method is no longer used until a new starting point is found. This strategy avoids wasting computational resources on LMA searches that are unlikely to improve the solution.

4.8 Strategies for using the VML code

The VML code can be used in a variety of ways with varying levels of user intervention. As a general rule, a reduction in user intervention results in an increase in the computer time required to fit the model. The strategy that requires the least amount of the analyst's time involves simply instructing the VML code to simultaneously fit all of the required parameters to all of the available laboratory data and using wide limits on the minimum and maximum allowable values for each of the parameters. This strategy is tantamount to searching a very large parameter space and can require significant computational resources for complex models such as the HRBM model. Using

the aforementioned strategy as a starting point, more effective strategies can be developed by finding methods of reducing the size of the parameter space that must be searched.

An effective method of reducing the size of the search space is to reduce the limits on the minimum and maximum allowable values for some of the parameters. For instance, tighter limits on the allowable values of a parameter can be determined by manually running the driver code in VML while varying a single parameter to get a feel for the effect of a given parameter on the stress/strain path of interest. Another method of establishing tighter limits on the allowable values is to allow the optimization module to obtain initial values of a reduced parameter set by fitting a reduced set of the laboratory data. For example, obtain initial values of the parameters that control the volumetric boundaries by fitting just the laboratory data for a hydrostatic compression experiment, and then use limits that allow those values to vary by plus or minus ~ten percent during the full-up optimization run. These fitting strategies usually require a more thorough understanding of the model and can require a significant amount of the analyst's time, but they do offer more control over the fitting process.

The VML code also allows the user to exert more control over the fitting process by specifying a weighting factor for each test as well as a weighting factor for each individual data point in a given test. Therefore, if the material model under consideration is not able to fit all of the laboratory experiments with one set of parameters or the entire stress-strain curve of a given experiment, the user can encourage the code to select a set of parameters that fit the most critical laboratory experiments and/or the most important region, i.e., loading versus unloading, of the stress-strain curves.

5. Model response in driver code

In this section the fidelity of a HRBM model fit to WES5000 concrete is examined by comparing the driver code simulations to the laboratory data used to fit the model parameters in the VML code.

Fig. 8 shows comparisons between driver simulations and the response observed in a UX experiment. Fig. 8(a) shows the comparison for the pressure-volume response observed in the UX experiment. Fig. 8(b) shows a comparison of the axial stress versus axial strain behavior predicted in the UX

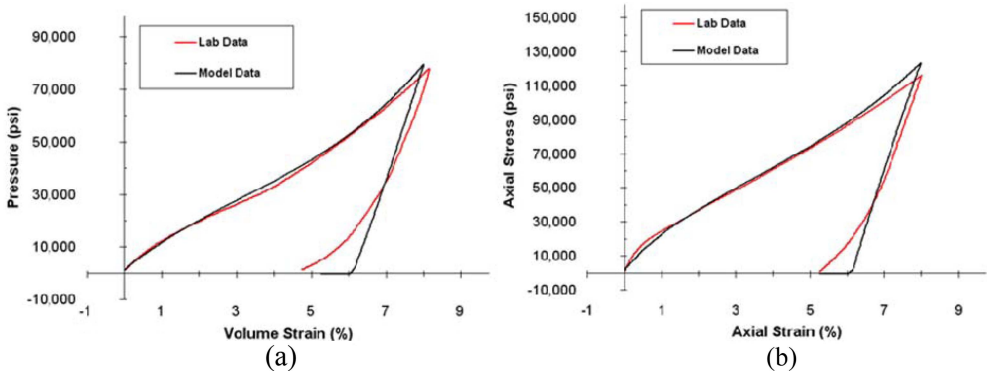

Fig. 8 Comparisons between VML driver simulations and data for a UX experiment; (a) pressure-volume behavior and (b) axial stress versus axial strain behavior

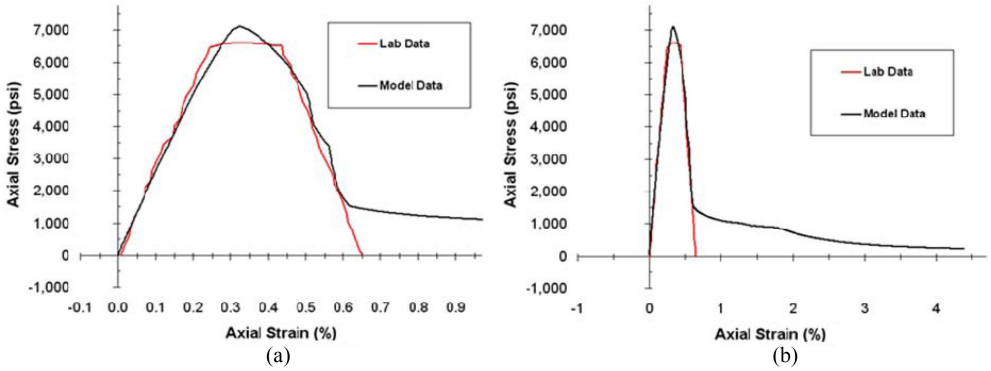

Fig. 9 Comparisons between VML driver simulations and data for a UC experiment; (a) close-up of comparison and (b) behavior at larger strains

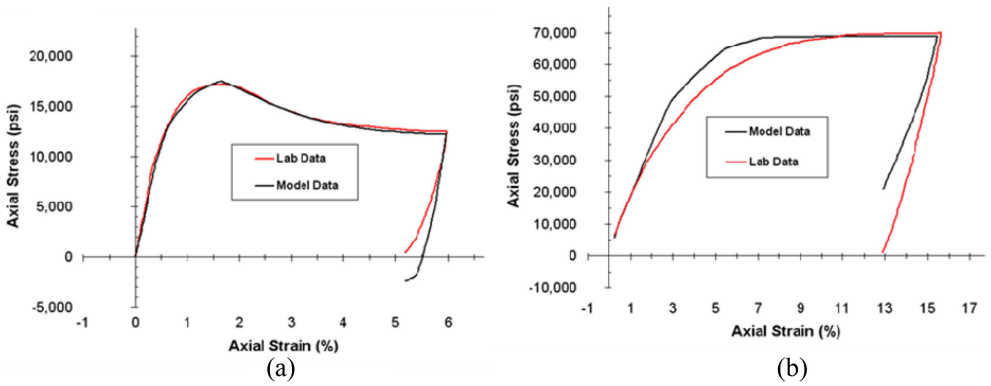

Fig. 10 Comparisons between VML driver simulations and data for TXC experiments; (a) confining pressure of 2.9 ksi and (b) confining pressure of 58 ksi

simulation with the response observed in the UX experiment. In both cases, the simulation and the experimental data are in close agreement. It is our experience that it is rare for a material model to be able to match both of those data sets for the UX test. Since the pressure-volume and the axial stress versus axial strain simulations are both in good agreement with the data, this also guarantees a reasonable prediction of the stress path (stress difference versus pressure) for the UX test.

Fig. 9 shows comparisons between the driver simulation and the experimental data for a UC experiment. Fig. 9(a) shows a close-up of the comparison to illustrate the high-fidelity of the simulation and Fig. 9(b) shows the response at larger strains. Note that the stress approaches zero as the strains become large.

Fig. 10 shows comparisons between simulations and experiments for two TXC experiments. Fig. 10(a) shows the comparison for a low-pressure TXC experiment conducted at a confining pressure of 2.9 ksi, and Fig. 10(b) shows the comparison for a high-pressure TXC experiment conducted at a confining pressure of 58 ksi. It is important to note that the HRBM model is able to accurately model the behavior observed in both low- and high-pressure TXC experiments. This capability is critical to obtaining high-fidelity predictions of boundary value problems of interest, such as projectile penetration (Frank and Adley 2007). It is also important to note that, due to the inclusion

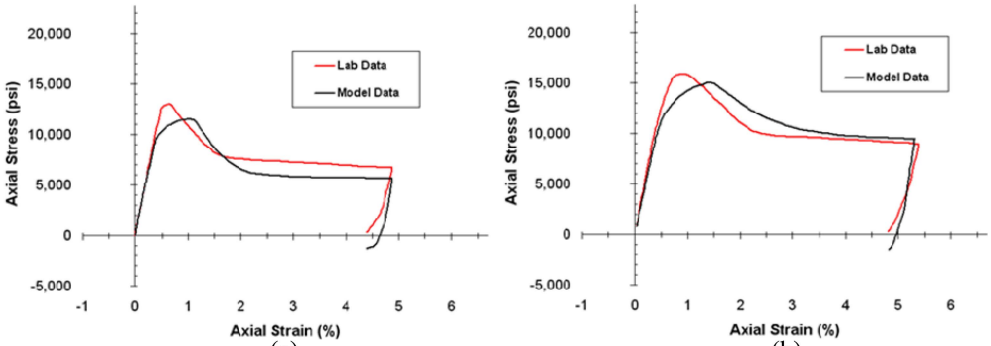

Fig. 11 Comparisons between VML driver simulations and data for TXC experiments; (a) confining pressure of 1 ksi and (b) confining pressure of 2 ksi

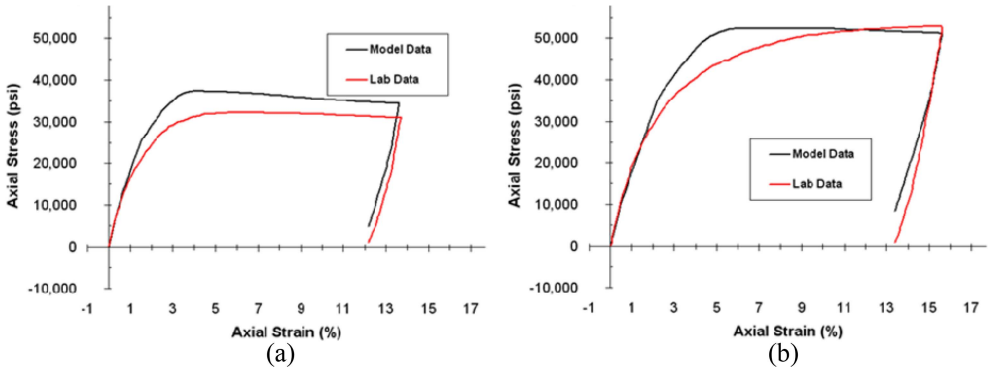

Fig. 12 Comparisons between VML driver simulations and data for TXC experiments; (a) confining pressure of 14.5 ksi and (b) confining pressure of 29 ksi

of a term that is a function of the volumetric strain in Eq. (7) and Eq. (8), the HRBM model is able to simulate the abrupt softening observed in the UC test shown in Fig. 9 as well as the more gradual softening observed in Fig. 10(a).

Fig. 11 shows comparisons between simulations and experiments for two low-pressure TXC experiments. Fig. 12 shows comparisons between simulations and experiments for two medium-pressure TXC experiments. The agreement shown in Figs. 11 and 12 is more than satisfactory, but it is not as close as the agreement obtained in the previous figures. This can be explained in part by plotting the peak stresses from all of the TXC experiments in stress difference versus pressure space as shown in Fig. 13. Specifically, there is a dip in the TXC failure data that defines the failure surface shown in Fig. 13, i.e., due to the resulting irregular shape of the failure surface, the current model cannot perfectly match the peaks of all of the TXC experiments.

Fig. 14 shows a comparison between the driver simulation and the experimental data for a DP experiment. It should be noted that, only the peak stress was obtained in the experiment, i.e., the post-peak softening data was not available. Therefore, we introduced a typical post-peak softening response from alternative data (Cargile 1999) in order to produce a material fit using the VML code. Unfortunately, a lack of post-peak softening data for tensile experiments is typical of most experimental data.

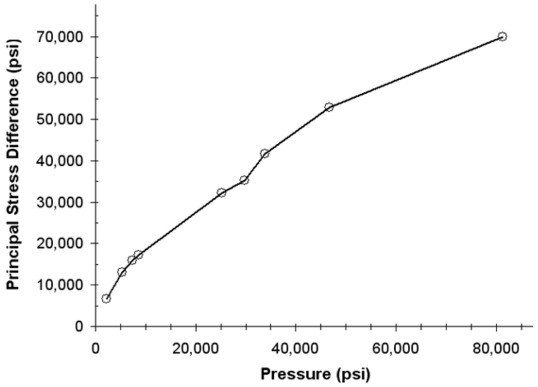

Fig. 13 The peak stresses from all of the TXC experiments plotted in principal stress difference versus pressure space to reveal the shape of the failure surface

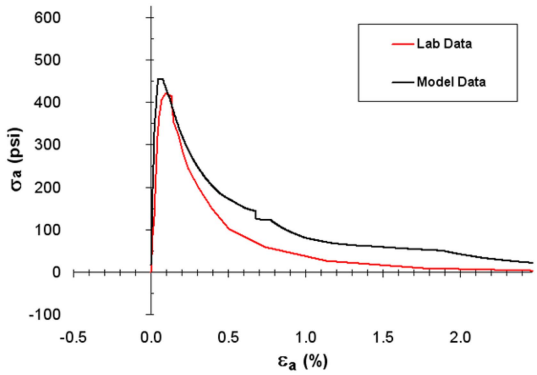

Fig. 14 Comparison between VML driver simulation and "hypothetical" data for a DP experiment

6. Conclusions

The HRBM model is capable of producing high-fidelity simulations of material property experiments, and capturing many important aspects of concrete behavior such as the brittle-to-ductile transition observed in TXC experiments conducted at different confining pressures. This capability of the HRBM model to accurately model both low- and high-pressure TXC behavior is critical to obtaining high-fidelity simulations of boundary problems of interest, such as projectile perforation events. Since the HRBM model shares the same framework as the M4 model it is also able to model other complex behaviors such as the vertex effect and coupling between deviatoric and volumetric behaviors (Bazant *et al.* 2000). The HRBM fit to WES5000 concrete presented in this paper, and its comparison to various material property data, shows significant promise for increasing the fidelity of projectile perforation events. This potential is explored in a companion paper that presents projectile penetration simulations conducted with the HRBM model as well as comparisons to penetration experiments.

Acknowledgements

The research documented herein was performed at the U.S. Army Engineer Research and Development Center, Geotechnical and Structures Laboratory. Permission to publish was granted by Director, Geotechnical and Structures Laboratory.

References

Adley, M.D., Frank, A.O., Danielson, K.T., Akers, S.A. and O'Daniel, J.L. (2010), "The virtual penetration laboratory: new developments for projectile penetration in concrete", *Comput. Concrete*, **7**(2), 87-102.
Akers, S.A., Adley, M.D. and Cargile, J.D. (1995), "Comparison of constitutive models for geologic materials

used in penetration and ground shock calculations", Proceedings of the 7th International Symposium on the Interaction of Conventional Munitions with Protective Structures, Mannheim FRG.
Bazant, Z.P., Caner, F.C., Carol, I., Adley, M.D. and Akers, S.A. (2000), "Microplane model M4 for concrete, I: formulation with work-conjugate deviatoric stress", *J. Eng. Mech.-ASCE*, **126**(9), 944-953.
Bazant, Z.P., Xiang, Y. and Prat, P.C. (1996), "Microplane model for concrete: I. Stress-strain boundaries and finite strain", *J. Eng. Mech.-ASCE*, **122**(3), 245-254.
Bazant, Z.P., Xiang, Y., Adley, M.D., Prat, P.C. and Akers, S.A. (1996), "Microplane model for concrete: II. Data delocalization and verification", *J. Eng. Mech.-ASCE*, **122**(3), 255-262.
Bazant, Z.P. and Oh, B.H. (1986), "Efficient numerical integration on the surface of a sphere", *ZAMM.-Z. Angew. Math. Me*., **66**(1), 37-49.
Caner, F.C. and Bazant, Z.P. (2000), "Microplane model M4 for concrete. II: algorithm and calibration", *J. Eng. Mech.-ASCE*, **126**(9), 954-961.
Cargile, J.D. (1999), "Development of a constitutive model for numerical simulations of projectile penetration into brittle geomaterials", Technical Report SL-99-11, U.S. Army Engineer Research and Development Center, Vicksburg, MS.
Danielson, K.T., Adley, M.D. and O'Daniel, J.L. (2010), "Numerical procedures for extreme impulsive loading on high strength concrete structures", *Comput. Concrete*, **7**(2), 159-167.
Frank, A.O., Adley, M.D., Danielson, K.T. and McDevitt, J.S. (2010), "The high-rate brittle microplane concrete model: Part II: application to projectile perforation of concrete slabs", *Comput. Concrete.*
Frank, A.O. and Adley, M.D. (2007), "On the importance of a three-invariant model for simulating the perforation of concrete slabs", Proceedings of the 78th Shock and Vibration Symposium, Philadelphia, PA, 4-8.
Frew, D.J., Cargile, J.D. and Ehrgott, J.Q. (1993), "WES Geodynamics and projectile penetration research facilities", Proceedings of the Symposium on Advances in Numerical Simulation Techniques for Penetration and Perforation of Solids, 1993 ASME Winter Annual Meeting, New Orleans, LA, 28.
Furukawa, T., Sugata, T., Yoshimura, S. and Hoffman, M. (2002), "An automated system for simulation and parameter identification of inelastic constitutive models", *Comput. Meth. Appl. Mech. Eng.*, **191**(21-22), 2235-2260.
Littlefield, D., Walls, K.C. and Danielson, K.T. (2010), "Integration of the microplane constitutive model into the EPIC code", *Comput. Concrete.*, **7**(2), 145-158.
Marquardt, D. (1963), "An algorithm for least-squares estimation of nonlinear parameters", *SIAM J. Appl. Math*., **11**(2), 431-441.
Ožbolt, J., Periškic, G., Reinhardt, H.F. and Eligehausen, R. (2008), "Numerical analysis of spalling of concrete cover at high temperature", *Comput. Concrete*, **5**(4), 279-293.
Ožbolt, J., Kozar, I., Eligehausen, R. and Periškic, G. (2005), "Three-dimensional FE analysis of headed stud anchors exposed to fire", *Comput. Concrete*, **2**(4), 249-266.
Parichatprecha, R. and Nimityongskul, P. (2009), "An integrated approach for optimum design of HPC mix proportion using genetic algorithm and artificial neural networks", *Comput. Concrete*, **6**(3), 253-268.
Roth, J.M., Slawson, T.R. and Flores, O.G. (2010), "Flexural and tensile properties of a glass fiber-reinforced ultra-high-strength concrete: An experimental, micromechanical and numerical study", *Comput. Concrete,* **7**(2), 169-190.
Williams, E.M., Graham, S.S., Akers, S.A., Reed, P.A. and Rushing, T.S. (2010), "Constitutive property behavior of an ultra-high-performance concrete with and without steel fibers", *Comput. Concrete*, **7**(2), 191-202.

CC